Check for updates

Visible-light-driven hydrogen evolution using calcium titanate codoped with aluminium, antimony, magnesium, and rhodium, loaded with a platinum (core)–chromia (shell) cocatalyst†

Tomoya Ota,[a] Ryota Tomizawa,[b] Tomoya Nagano,[b] Koji Hayashi[b] and Shigeru Ikeda [ID] *[ac]

Calcium titanate codoped with Al^{3+}, Sb^{5+}, Mg^{2+}, and Rh (Rh^{3+} or Rh^{4+}), prepared *via* the flux method, showed efficient visible-light-driven H_2 evolution using methanol as a hole scavenger. Loading Pt (core)–Cr_2O_3 (shell) nanoparticles as a cocatalyst enhanced the performance, with an apparent quantum yield of 7.1% being achieved at 420 nm.

Sunlight-induced water splitting using mixed-oxide semiconductor photocatalysts has gained attention for its potential in hydrogen (H_2) production, an alternative energy source for fossil fuels.[1] Efficient utilization of sunlight requires photocatalysts with narrow band gaps to absorb visible light. However, many mixed-oxide semiconductors have a deep valence band maximum (VBM) because valence bands of such mixed-oxide semiconductors consist of oxygen 2p orbitals,[2] making it challenging to achieve a sufficient reduction potential for H_2 evolution. One approach is to hybridize oxygen 2p orbitals with other atomic orbitals, creating a shallower VBM. Materials such as oxynitrides,[3–5] oxysulfides,[6,7] and oxyhalides[8,9] have demonstrated visible-light-driven H_2 production.

Another approach to provide photocatalytic activity under visible-light irradiation is doping of a transition metal cation to form a mid-gap state (or an impurity level) in the forbidden band of a wide-gap semiconductor compound. Although such a concept used to be unpromising because it was thought that such an energy state would facilitate recombination of photoexcited carriers,[10] several reports have shown that visible light-driven photocatalytic reactions are induced over transition metal-doped photocatalysts based on wide-gap host compounds including $SrTiO_3$,[11–20] $BaTiO_3$,[21] $NaTaO_3$,[22] and $ZnGa_2O_4$.[23]

Among them, $SrTiO_3$ is a promising host compound for photocatalytic H_2 evolution under visible light. Since the first example of doping trivalent rhodium ion (Rh^{3+}) to substitute the B site (Ti^{4+}) in the crystal lattice of $SrTiO_3$ ($SrTiO_3$:Rh),[11] several photocatalytic materials using various kinds of dopants have been reported by Kudo *et al.*[12–16,20] Further improvements were achieved by applying a codoping concept that is charge compensation of a doped cation by a codopant, such as pentavalent antimony ion (Sb^{5+}) at the Ti^{4+} site ($SrTiO_3$:Sb,Rh)[12,13] or tetravalent lanthanum ion (La^{3+}) at the Sr^{2+} site ($SrTiO_3$:La,Rh).[19,20] These strategies stabilize the trivalent state of the doped rhodium, leading to significant enhancement of photocatalytic H_2 evolution activity.

Calcium titanate ($CaTiO_3$), a perovskite compound with a band gap of 3.5 eV,[24] has potential as a host material for photocatalysts, but there has been limited success in the use of $CaTiO_3$ compared to $SrTiO_3$. Compared to $SrTiO_3$, the wider band gap of $CaTiO_3$, along with its structural properties of $CaTiO_3$, make it suitable for transition-metal doping. However, there have been few reports on the application of $CaTiO_3$ as the host material, and high photocatalytic activity has not been achieved.[25] In this study, visible-light-responsive $CaTiO_3$:Rh photocatalysts were developed with codoping of Al^{3+}, Sb^{5+}, and Mg^{2+} at the Ti^{4+} site ($CaTiO_3$:Al,Sb,Mg,Rh). In addition, a cocatalyst of Pt (core)–Cr_2O_3 (shell) nanoparticles was developed to further boost H_2 evolution efficiency. The optimized $CaTiO_3$:Al,Sb,Mg,Rh system achieved impressive apparent quantum yields (AQYs) of 8.0% at 400 nm and 7.1% at 420 nm in a sacrificial H_2 evolution.

We synthesized powder samples of $CaTiO_3$ doped with Al^{3+} ($CaTiO_3$:Al), $CaTiO_3$:Al codoped with Rh (Rh^{3+} or Rh^{4+}) ($CaTiO_3$:Al,Rh), $CaTiO_3$:Al,Rh codoped with Sb^{5+} ($CaTiO_3$:Al,Sb,Rh), and $CaTiO_3$:Al,Sb,Rh codoped with Mg^{2+} ($CaTiO_3$:Al,Sb,Mg,Rh) using the flux method in molten $CaCl_2$ (details in ESI†). All of the samples contained Al^{3+} derived from the alumina crucible used during the flux treatment, while the other dopants were intentionally introduced during synthesis. Powder XRD analyses revealed that all samples exhibited orthorhombic $CaTiO_3$

[a] *Department of Chemistry, Konan University, 9-1 Okamoto, Higashinada-ku, Kobe, Hyogo 658-8501, Japan. E-mail: s-ikeda@konan-u.ac.jp*

[b] *Carbon Neutral Development Division, Toyota Motor Corporation, 1200 Mishuku, Susono, Shizuoka 410-1193, Japan*

[c] *Institute for Energy Conversion Materials, Konan University, 9-1 Okamoto, Higashinada-ku, Kobe, Hyogo 658-8501, Japan*

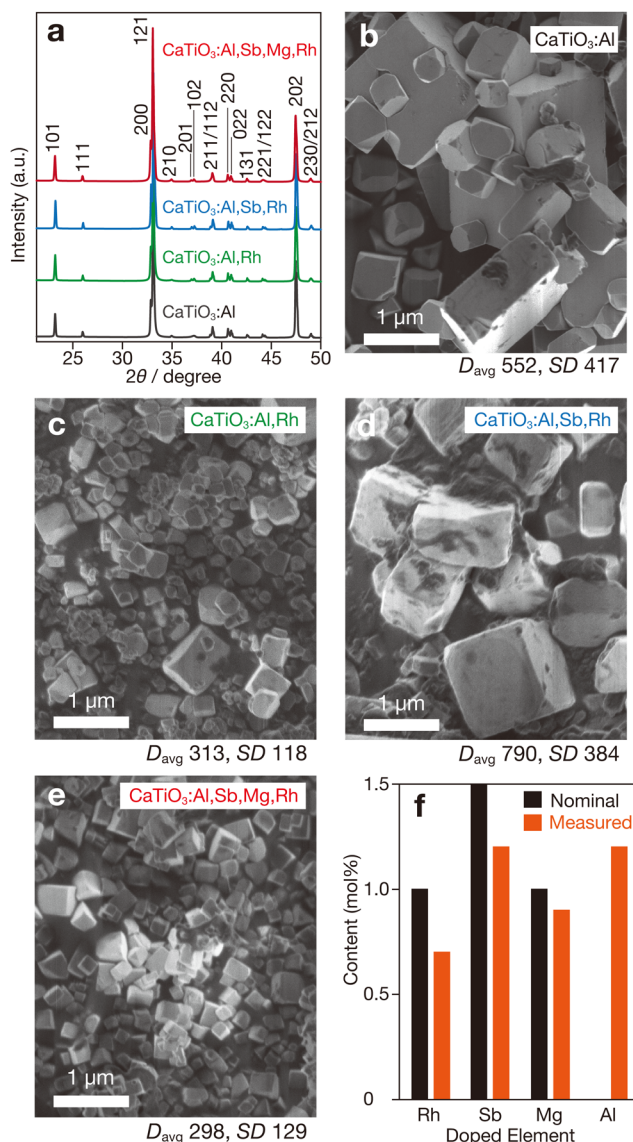† Electronic supplementary information (ESI) available. See DOI: https://doi.org/10.1039/d5ma00098j

Fig. 1 Structural characterizations of doped CaTiO₃ samples. (a) XRD patterns and SEM images of (b) CaTiO$_3$:Al, (c) CaTiO$_3$:Al,Rh, (d) CaTiO$_3$:Al,Sb,Rh and (e) CaTiO$_3$:Al,Sb,Mg,Rh, (f) nominal and measured amounts of doped elements in CaTiO$_3$:Al,Sb,Mg,Rh. D_{avg} and SD values in panels (b)–(e) denote average diameter and standard deviation in nanometre units, respectively.

perovskite structures (ICSB 1000022) with no detectable impurities (Fig. 1a), suggesting successful incorporation of dopants into the crystalline lattice of the host CaTiO$_3$. The ionic radii of the dopants used (Rh^{3+}: 66.5 pm (or Rh^{4+}: 60.0 pm), Al^{3+}: 53.5 pm, Sb^{5+}: 60.0 pm, and Mg^{2+}: 72.0 pm) are significantly smaller than the ionic radius of A site Ca^{2+} (134 pm) but comparable to the B-site Ti^{4+} radius (60.5 pm). Thus, these dopants should occupy the B-site positions. Furthermore, no appreciable shifts in the diffraction peaks of CaTiO$_3$ were observed, indicating negligible lattice expansion or contraction due to doping.

In contrast to the crystallographic results, the morphological characteristics of samples with different compositions showed

notable variations. The CaTiO$_3$:Al sample consisted of cubic or rectangular particles with relatively large sizes (Fig. 1b). The exposed surfaces were likely facets oriented along the {100} and {001} directions, suggesting that each particle would be in a single-crystalline state. For the CaTiO$_3$:Al,Rh sample, a significant reduction in particle size was observed (Fig. 1c), indicating that rhodium doping suppressed particle growth. Measurements of average particle size (D_{avg}) and standard deviation (SD) (Fig. S1, ESI†) revealed reductions of more than half in both parameters compared to the CaTiO$_3$:Al sample. Conversely, substantial particle growth was observed in the antimony-codoped sample (CaTiO$_3$:Al,Sb,Rh), with a larger D_{avg} than that of CaTiO$_3$:Al, as shown in Fig. 1d. On the other hand, the sample further codoped with magnesium (CaTiO$_3$:Al,Sb,Mg,Rh) exhibited smaller particles with relatively uniform size distributions (Fig. 1e). Although the underlying mechanisms remain unclear, these results suggest that particle size depends on the valency of the dopant. The high-valent Sb^{5+} cations promoted particle growth, whereas the low-valent Mg^{2+} cation appeared to suppress particle growth. ICP measurements (Fig. 1f) confirmed that the intentionally added dopants were present in amounts exceeding half of their respective nominal contents, while the Al^{3+} component, leached from the alumina crucible, was present in comparable quantities.

Photocatalytic activity of doped CaTiO$_3$ samples for water reduction in the presence of methanol as a sacrificial hole scavenger under visible-light irradiation (>400 nm) was evaluated. The samples were loaded with a nanoparticulate platinum (Pt) cocatalyst by using the photodeposition method (details in ESI†). Since the Pt was found to be the most effective of the known cocatalysts for the SrTiO$_3$-based doped photocatalytic system[11–13,19,20] (data not shown), the effect of the Pt cocatalyst was focused in this study. Fig. 2a shows the amounts of H$_2$ evolved as a function of photoirradiation time for these photocatalysts. The CaTiO$_3$:Al-based photocatalyst showed almost no H$_2$ evolution due to its lack of photoabsorption in the visible light region (see below). In contrast, photocatalysts containing rhodium exhibited visible light-driven H$_2$ evolution. Compared to the CaTiO$_3$:Al,Rh-based photocatalyst, codoping with Sb^{5+} significantly increased the H$_2$ evolution rate. The activity was further enhanced in the CaTiO$_3$:Al,Sb,Mg,Rh-based photocatalyst.

Instead of conventional Pt cocatalysts, a Pt (core)–chromia (shell) (Pt/Cr$_2$O$_3$) cocatalyst was used for the sacrificial H$_2$ evolution system. This cocatalyst was prepared by successive reductive photodeposition of aqueous precursors, similar to the method used for Rh (core)–Cr$_2$O$_3$ (shell) (Rh/Cr$_2$O$_3$) cocatalysts, which are known to be effective in several photocatalysts for overall water splitting.[5,26,27] Fig. 2b shows typical time courses of H$_2$ evolution for Pt/Cr$_2$O$_3$-loaded CaTiO$_3$:Al,Rh, CaTiO$_3$:Al,Sb,Rh, and CaTiO$_3$:Al,Sb,Mg,Rh photocatalysts. Compared to photocatalysts with conventional Pt cocatalysts, significant improvements in H$_2$ evolution were observed for the photocatalysts. Notably, the CaTiO$_3$:Al,Sb,Mg,Rh-based photocatalyst exhibited a substantial increase in the H$_2$ production rate. The activity was continued for a further 2 runs without any appreciable degradation (Fig. S2, ESI†).
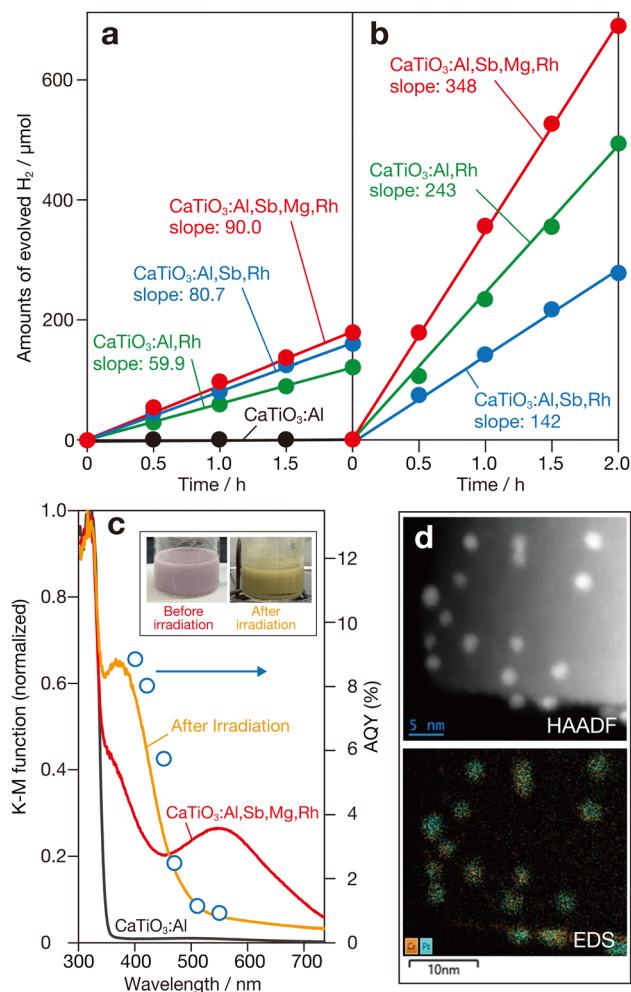
Fig. 2 Amount of evolved H_2 as a function of photoirradiation (>400 nm) duration from aqueous methanol solutions containing doped $CaTiO_3$ samples loaded with (a) Pt and (b) Pt (core)−Cr_2O_3 (shell) (Pt/Cr_2O_3) cocatalysts. Slope values denote the rate of H_2 evolution (μmol h^{-1}). (c) DR spectra of $CaTiO_3$:Al, $CaTiO_3$:Al,Sb,Mg,Rh, and a suspension of Pt/Cr_2O_3-loaded $CaTiO_3$:Al,Sb,Mg,Rh after photoirradiation. Dependence of AQYs for the sacrificial H_2 evolution on wavelength of incident photons is also plotted. The inset shows photographs of a suspension containing $CaTiO_3$:Al,Sb,Mg,Rh (labelled Before irradiation) and that loaded with Pt/Cr_2O_3 cocatalyst obtained after photodeposition process (labelled after irradiation). (d) HAADF scanning TEM (upper) and EDS elemental mapping (lower) images of loaded Pt/Cr_2O_3 cocatalyst.

The apparent quantum yields (AQYs) of this photocatalyst were 8.0% at 400 nm and 7.1% at 420 nm. To the best of our knowledge, these results represent the first demonstration of significantly high photocatalytic performance in an Rh-doped photocatalytic system using a host semiconductor material other than $SrTiO_3$.

Fig. 2c shows diffuse reflection (DR) spectra of $CaTiO_3$:Al and $CaTiO_3$:Al,Sb,Mg,Rh samples. The $CaTiO_3$:Al sample exhibited fundamental photoabsorption in the ultraviolet region, with a photoabsorption onset at 355 nm. From this onset, the band-gap energy was estimated to be approximately 3.5 eV, being consistent with the previously reported value for undoped $CaTiO_3$.[24] In contrast, the $CaTiO_3$:Al,Sb,Mg,Rh sample exhibited additional photoabsorption extending from the ultraviolet

region into the visible light region. This additional absorption can be divided into two components: a shoulder component near the band-gap absorption of $CaTiO_3$, centered around 390 nm and a broad absorption band in the visible region, centered around 560 nm. Based on results of previous studies on Rh-doped photocatalysts using $SrTiO_3$,[11,13] these two absorption bands are attributed to transitions related to trivalent rhodium ion (Rh^{3+}) and tetravalent rhodium ion (Rh^{4+}). The Rh^{3+} dopant acts as an electron donor, with its absorption band corresponding to transitions from the donor level introduced by Rh^{3+} to the conduction band, which facilitates water reduction to H_2. In contrast, the Rh^{4+} dopant forms a deep acceptor level that can negatively impact photocatalytic H_2 evolution by promoting recombination of photogenerated charge carriers. Based on the charge compensation mechanism, codoping with pentavalent antimony ion (Sb^{5+}) at the B site of $CaTiO_3$ (Ti^{4+}) stabilizes the trivalent state of the rhodium component at the B site. In contrast, doping with low-valent aluminium and magnesium ions (Al^{3+} and Mg^{2+}) at the B site increases the proportion of Rh^{4+} species to compensate for the charge imbalance caused by these ions. As a result, the DR spectrum of the $CaTiO_3$:Al,Sb,Mg,Rh sample showed noticeable absorption attributed to the Rh^{4+}-derived deep acceptor band, whereas the Rh^{3+}-related transition band was not significantly enhanced. The greyish-purple appearance of the sample further indicates the dominant presence of the Rh^{4+} component in the material.

As observed in the photocatalytic H_2 evolution under visible-light irradiation over Rh-doped $SrTiO_3$ photocatalysts,[11,12] the color of the suspension changed to yellow during the photodeposition process of Pt or Pt/Cr_2O_3 cocatalysts (inset of Fig. 2c), though the color changed back to the original color upon exposure to air due probably to the above-mentioned charge imbalance of B site cation. Compared to the DR spectrum of the bare $CaTiO_3$:Al,Sb,Mg,Rh sample, the DR spectrum of the suspension obtained after 3 h of light irradiation with a Xe lamp (>400 nm) and measured under argon (Ar) (details in ESI†) showed an increase in the Rh^{3+}-related band and a corresponding decrease in the Rh^{4+}-related band, as depicted in Fig. 2c. This color change suggests the occurrence of reductive activation of doped rhodium species in the sample. Furthermore, the plots of apparent quantum yields (AQYs) as a function of incident photon wavelength were consistent with the photoabsorption characteristics of the yellow-colored suspension, reinforcing this interpretation. Since the suspensions containing $CaTiO_3$:Al,Rh and $CaTiO_3$:Al,Sb,Rh exhibited nearly the same yellow color after photoirradiation (Fig. S3, ESI†), it is considered that similar photoactivation occurred in these samples as in the $CaTiO_3$:Al,Sb,Mg,Rh sample. Although detailed quantitative analyses have not yet been conducted, the highest activity observed for the $CaTiO_3$:Al,Sb,Mg,Rh-based photocatalysts is likely due to significant suppression of particle growth (Fig. 1), as well as stabilization of trivalent rhodium species (Rh^{3+}) induced by co-doping with pentavalent antimony ions (Sb^{5+}).

To investigate the structural properties of the Pt/Cr_2O_3 cocatalyst, TEM-EDS measurements were performed using the

Pt/Cr$_2$O$_3$-loaded CaTiO$_3$:Al,Sb,Mg,Rh sample recovered after the sacrificial H$_2$ evolution reaction. A low-magnification secondary electron (SE) scanning image revealed homogeneous deposition of nanoparticles across the entire surface of the rectangular CaTiO$_3$:Al,Sb,Mg,Rh particles (Fig. S4, ESI†). Bright-field (BF) and high-angle annular dark field (HAADF) scanning TEM images confirmed the presence of Pt in the observed nanoparticles (Fig. S4, ESI† and Fig. 2d). As shown in the same figures, corresponding EDS elemental mapping images showed overlapping signals of Pt and chromium (Cr) at the locations of the nanoparticles. Since Pt and Cr$_2$O$_3$ were sequentially deposited by photoreduction of their respective precursor ions (i.e., PtCl$_4^{2-}$ and CrO$_4^{2-}$), these results confirm the formation of Cr$_2$O$_3$ layers over the initially deposited Pt nanoparticles, i.e., the creation of Pt (core)–Cr$_2$O$_3$ (shell) cocatalysts resulted in significant enhancement of H$_2$ evolution.

For the Rh/Cr$_2$O$_3$ cocatalyst used in several photocatalysts for overall water splitting, the Cr$_2$O$_3$ surface layer is known to prevent O$_2$ from reaching the surface of the inner Rh nanoparticle core, effectively suppressing the backward reaction of water splitting.[28] A similar effect of the Cr$_2$O$_3$ layer on Pt cocatalysts has also been proposed.[5] Since the current system involves a sacrificial reaction using methanol as a hole scavenger, the suppression of the reverse reaction in overall water splitting cannot fully account for the observed phenomenon. According to recent studies on the electrocatalytic properties of Rh/Cr$_2$O$_3$ nanoparticles supported on conductive substrates,[29] the Cr$_2$O$_3$ layer may facilitate proton (H$^+$) access to the Pt core surface while inhibiting the approach of other reagents and ions. If the Cr$_2$O$_3$ shell indeed has such effects, there may be potential to enhance catalytic activity by optimizing its thickness. This is being considered for future investigation.

In this study, we explored the potential of CaTiO$_3$ as a host material for Rh-doped photocatalysts used in H$_2$ evolution under visible-light irradiation. Significant performance enhancement was achieved by using Rh-doped CaTiO$_3$ codoped with Al^{3+}, Sb^{5+}, and Mg^{2+} cations, loaded with the Pt/Cr$_2$O$_3$ cocatalyst: the use of the photocatalyst resulted in a high AQY of 7.1% at 420 nm among the doped photocatalytic systems. Although the perovskite CaTiO$_3$ compound has not been extensively studied as a host material, it demonstrates considerable potential for further activity enhancement.

Author contributions

T. O. and S. I. directed and led the research. T. O. performed structural analyses and photocatalytic experiments. R. T., T. N., and K. H. performed TEM measurements and analyses. All the authors discussed the results. T. O. and S. I. wrote the manuscript.

Data availability

Experimental details and the data supporting this article have been included as part of the ESI.†

Conflicts of interest

The authors declare no conflict of interest.

Acknowledgements

Notes and references

1 (a) B. A. Pinaud, J. D. Benck, L. C. Seitz, A. J. Forman, Z. Chen, T. G. Deutsch, B. D. James, K. N. Baum, G. N. Baum, S. Ardo, H. Wang, E. Miller and T. F. Jaramillo, Energy Environ. Sci., 2013, 6, 1983; (b) D. M. Fabian, S. Hu, N. Singh, F. A. Houle, T. Hisatomi, K. Domen, F. E. Osterloh and S. Ardo, Energy Environ. Sci., 2015, 8, 2825.

2 A. Kudo and Y. Miseki, Chem. Soc. Rev., 2009, 38, 253.

3 W.-J. Chun, A. Ishikawa, H. Fujisawa, T. Takata, J. N. Kondo, M. Hara, M. Kawai, Y. Matsumoto and K. Domen, J. Phys. Chem. B, 2003, 107, 1798.

4 K. Maeda, K. Teramura, D. Lu, T. Takata, N. Saito, Y. Inoue and K. Domen, Nature, 2006, 440, 295.

5 K. Maeda, K. Teramura, D. Lu, N. Saito, Y. Inoue and K. Domen, Angew. Chem., Int. Ed., 2006, 45, 7806.

6 A. Ishikawa, T. Takata, J. N. Kondo, M. Hara, H. Kobayashi and K. Domen, J. Am. Chem. Soc., 2002, 124, 13547.

7 Q. Wang, M. Nakabayashi, T. Hisatomi, S. Sun, S. Akiyama, Z. Wang, Z. Pan, X. Xiao, T. Watanabe, T. Yamada, N. Shibata, T. Takata and K. Domen, Nat. Mater., 2019, 18, 827.

8 H. Fujito, H. Kunioku, D. Kato, H. Suzuki, M. Higashi, H. Kageyama and R. Abe, J. Am. Chem. Soc., 2016, 138, 2082.

9 X. Tao, Y. Zhao, L. Mu, S. Wang, R. Li and C. Li, Adv. Energy Mater., 2018, 8, 1701392.

10 S. Ikeda, N. Sugiyama, B. Pal, G. Marcí, L. Palmisano, H. Noguchi, K. Uosaki and B. Ohtani, Phys. Chem. Chem. Phys., 2001, 3, 267.

11 R. Konta, T. Ishii, H. Kato and A. Kudo, J. Phys. Chem. B, 2004, 108, 8992.

12 (a) Y. Sasaki, H. Nemoto, K. Saito and A. Kudo, J. Phys. Chem. C, 2009, 113, 17536; (b) H. Kato, Y. Sasaki, N. Shirakura and A. Kudo, J. Mater. Chem. A, 2013, 1, 12327.

13 K. Furuhashi, Q. Jia, A. Kudo and H. Onishi, J. Phys. Chem. C, 2013, 117, 19101.

14 R. Niishiro, S. Tanaka and A. Kudo, Appl. Catal., B, 2014, 150–151, 187.

15 S. Suzuki, H. Matsumoto, A. Iwase and A. Kudo, Chem. Commun., 2018, 54, 10606.

16 T. Ishii, H. Kato and A. Kudo, J. Photochem. Photobiol. A, 2004, 163, 181.

17 P. Reunchan, S. Ouyang, N. Umezawa, H. Xu, Y. Zhang and J. Ye, J. Mater. Chem. A, 2013, 1, 422117.

18 K. Sayama, K. Mukasa, R. Abe, Y. Abe and H. Arakawa, *Chem. Commun.*, 2001, 2416.

19 Q. Wang, T. Hisatomi, S. S. K. Ma, Y. Li and K. Domen, *Chem. Mater.*, 2014, **26**, 4144.

20 Q. Wang, T. Hisatomi, Q. Jia, H. Tokudome, M. Zhong, C. Wang, Z. Pan, T. Takata, M. Nakabayashi, N. Shibata, Y. Li, I. D. Sharp, A. Kudo, T. Yamada and K. Domen, *Nat. Mater.*, 2016, **15**, 611.

21 K. Maeda, *ACS Appl. Mater. Interfaces*, 2014, **6**, 2167.

22 X. Zhou, J. Shi and C. Li, *J. Phys. Chem. C*, 2011, **115**, 8305.

23 N. Kumagai, L. Ni and H. Irie, *Chem. Commun.*, 2011, **47**, 1884.

24 T. Kimijima, K. Kanie, M. Nakaya and A. Muramatsu, *CrystEngComm*, 2014, **16**, 5591.

25 (*a*) S. Nishimoto, M. Matsuda and M. Miyake, *Chem. Lett.*, 2006, **35**, 308; (*b*) J. S. Jang, P. H. Borse, J. S. Lee, K. T. Lim, O.-S. Jung, E. D. Jeong, J. S. Bae and H. G. Kim, *Bull. Korean Chem. Soc.*, 2011, **32**, 95; (*c*) R. Wang, S. Ni, G. Liu and X. Xu, *Appl. Catal., B*, 2018, **225**, 139.

26 T. Takata, J. Jiang, Y. Sakata, M. Nakabayashi, N. Shibata, V. Nandal, K. Seki, T. Hisatomi and K. Domen, *Nature*, 2020, **581**, 411.

27 S. Ikeda, R. Okamoto, A. Kimura, Y. Nakayasu, A. Yamakata, R. Tomizawa, T. Masuda and K. Nakatani, *Sustainable Energy Fuels*, 2024, **8**, 202.

28 M. Yoshida, K. Takanabe, K. Maeda, A. Ishikawa, J. Kubota, Y. Sakata, Y. Ikezawa and K. Domen, *J. Phys. Chem. C*, 2009, **113**, 10151.

29 T. Higashi, K. Seki, Y. Sasaki, Y. Pihosh, V. Nandal, M. Nakabayashi, N. Shibata and K. Domen, *Chem. – Eur. J.*, 2023, **29**, e20220458.